

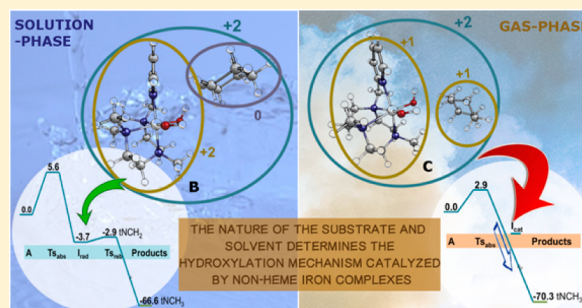
Computational Insight into the Mechanism of Alkane Hydroxylation by Non-heme Fe(PyTACN) Iron Complexes. Effects of the Substrate and Solvent

Verònica Postils, Anna Company, Miquel Solà,* Miquel Costas,* and Josep M. Luis*

Institut de Química Computacional i Catàlisi (IQCC) and Departament de Química, Universitat de Girona, Campus de Montilivi, 17071 Girona, Catalonia, Spain

S Supporting Information

ABSTRACT: The reaction mechanisms for alkane hydroxylation catalyzed by non-heme Fe^VO complexes presented in the literature vary from rebound stepwise to concerted highly asynchronous processes. The origin of these important differences is still not completely understood. Herein, in order to clarify this apparent inconsistency, the hydroxylation of a series of alkanes (methane and substrates bearing primary, secondary, and tertiary C–H bonds) through a Fe^VO species, [Fe^V(O)(OH)(PyTACN)]²⁺ (PyTACN = 1-(2'-pyridylmethyl)-4,7-dimethyl-1,4,7-triazacyclononane), has been computationally examined at the gas phase and in acetonitrile solution. The initial breaking of the C–H bond can occur via hydrogen atom transfer (HAT), leading to an intermediate where there is an interaction between the radical substrate and [Fe^{IV}(OH)₂(PyTACN)]²⁺, or through hydride transfer to form a cationic substrate interacting with the [Fe^{III}(OH)₂(PyTACN)]⁺ species. Our calculations show the following: (i) except for methane in the rest of the alkanes studied, the intermediate formed by R⁺ and [Fe^{III}(OH)₂(PyTACN)]⁺ is more stable than that involving the alkyl radical and the [Fe^{IV}(OH)₂(PyTACN)]²⁺ complex; (ii) in spite of (i), the first step of the reaction mechanism for all substrates is a HAT instead of hydride abstraction; (iii) the HAT is the rate-determining step for all analyzed cases; and (iv) the barrier for the HAT decreases along methane → primary → secondary → tertiary carbon. The second part of the reaction mechanism corresponds to the rebound process. Therefore, the stereospecific hydroxylation of alkane C–H bonds by non-heme Fe^V(O) species occurs through a rebound stepwise mechanism that resembles that taking place at heme analogues. Finally, our study also shows that, to properly describe alkane hydroxylation processes mediated by Fe^VO species, it is essential to consider the solvent effects during geometry optimizations. The use of gas-phase geometries explains the variety of mechanisms for the hydroxylation of alkanes reported in the literature.



I. INTRODUCTION

Reactions involving functionalization of alkane C–H bonds are of interest because they enable reactivity into otherwise inert molecules.^{1,2} Alkane hydroxylation processes (AHPs) have importance in enzymatic oxidations that participate in metabolic paths, xenobiotic detoxification, and biodegradation, among others.^{3–6} Furthermore, alkane C–H oxidation reactions find major interest in current organic synthesis.^{7,8} Particularly interesting are C–H oxidation processes mediated by iron-based species that occur with retention of the configuration at the hydroxylated carbon. Stereospecific hydroxylations find ample precedent in iron oxygenases, cytochrome P-450 being a paradigmatic case.³ However, they are difficult to reproduce with synthetic complexes because the combination of oxidants with iron compounds very easily results in the formation of Fenton-like free diffusing radical processes.^{8–14} The preparation of non-heme Fe^{IV}(O) complexes during the past decade has represented a major step forward, reproducing the chemistry taking place at non-heme iron-dependent oxygenases, and has

prompted the investigation of their reactivity in alkane C–H oxidation.^{15,16}

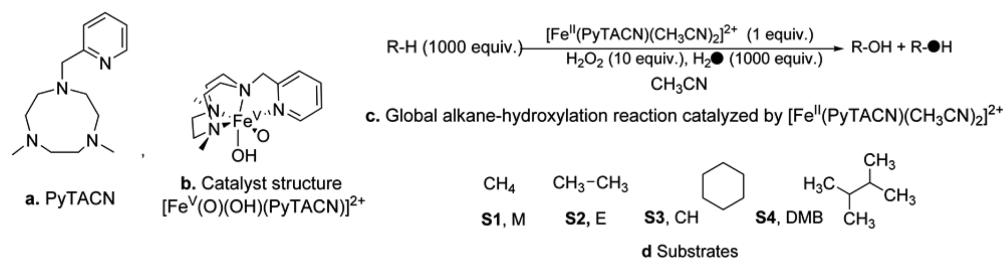
Non-heme Fe^{IV}(O) species have been shown to be capable of breaking the strong C–H bond of alkanes via a hydrogen atom transfer (HAT) reaction.^{17,18} Close investigation of the non-enzymatic reactions shows that long-lived carbon-centered radicals are produced after the initial HAT.^{19,20} Thus, these reactions fundamentally depart from stereoretentive processes. In parallel studies, a series of iron complexes containing aminopyridine ligands have been shown capable of mediating stereospecific C–H hydroxylation reactions upon reaction with hydrogen peroxide, and therefore their mechanism of action does not involve generation of free diffusing radicals.^{9–11,21}

Among the non-heme iron complexes that are catalytically active in AHPs we can mention the perferryl [Fe^V(O)(OH)(PyTACN)]²⁺ (PyTACN = 1-(2'-pyridylmethyl)-4,7-dimethyl-1,4,7-triazacyclononane) species, that is formed upon reaction of

Received: March 18, 2015

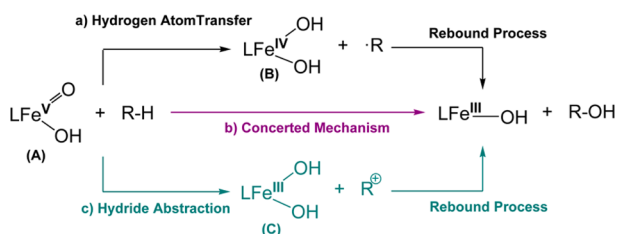
Published: August 19, 2015

Scheme 1. Ligand (a), Catalyst (b), and Substrates (d) Used in This Study, and Global Alkane Hydroxylation Reaction Catalyzed by the Studied Catalyst (c)



the $[\text{Fe}^{\text{II}}(\text{CF}_3\text{SO}_3)_2(\text{PyTACN})]$ catalyst with excess of H_2O_2 in acetonitrile (Scheme 1a–c). The capability of perferryl complexes to catalyze AHPs has been proven experimentally and computationally.^{22–24} This reaction occurs with stereo-retention at the hydroxylated carbon site, indicating that long-lived carbon centered radicals or cations are not involved. Other complexes studied in the literature that have also been proposed to involve $\text{Fe}^{\text{V}}(\text{O})$ species include: $[\text{Fe}^{\text{V}}(\text{O})(\text{OH})(\text{L})]^{2+}$ (where $\text{L} = \text{TPA}$ (TPA = tris(2-pyridylmethyl)amine) and related),^{21,25} $[\text{Fe}^{\text{V}}(\text{O})(\text{L})]^+$ (where $\text{L} = \text{dpaq}$ (dpaq = 2-[bis(pyridin-2-ylmethyl)]amino-*N*-quinolin-8-yl-acetamidate),²⁶ and $[\text{Fe}^{\text{V}}(\text{O})(\text{TAML})]^-$ (TAML = tetraamido macrocyclic ligand) and related.^{27–29} However, the reaction mechanisms for alkane oxidation processes catalyzed by $\text{Fe}^{\text{V}}(\text{O})$ complexes presented in literature show important differences among them, whose origin is not completely understood.^{23,25,29,30} In all cases reaction of the $\text{Fe}^{\text{V}}(\text{O})$ (A) species with an alkane starts with a HAT from the C–H bond by the iron-oxo group and then several different hypothetical pathways are proposed (Scheme 2). The most

Scheme 2. Proposed Mechanisms for Alkane Hydroxylation via $\text{Fe}^{\text{V}}(\text{O})(\text{OH})(\text{L})$ Catalysts



accepted one is the “rebound mechanism” where the HAT forms an alkyl radical intermediate (R^\bullet) that interacts with a bishydroxo $\text{Fe}^{\text{IV}}(\text{OH})_2$ species (B) that leads to the final hydroxylated products (path a in Scheme 2). This rebound mechanism for alkane hydroxylation catalyzed by non-heme $\text{Fe}^{\text{V}}(\text{O})$ species was proposed in previous density functional theory (DFT) studies as, for instance, in a work of methane and acetonitrile hydroxylation by $[\text{Fe}^{\text{V}}(\text{O})(\text{OH})(\text{TPA})]^{2+}$.²⁵

A second proposed mechanism involves direct formation of the hydroxylated products through a concerted highly asynchronous mechanism (path b in Scheme 2). The transition state in this single step process is given by the HAT, which is followed by the C–O bond formation without the generation of any intermediate. For instance, this asynchronous concerted mechanism was proposed for the cyclohexane hydroxylation catalyzed by $[\text{Fe}^{\text{V}}(\text{O})(\text{OH})(\text{L})]^{2+}$ ($\text{L} =$ tetradentate bispidine ligand)³² and by $[\text{Fe}^{\text{V}}(\text{O})(\text{OH})(\text{PyTACN})]^{2+}$.²³ Finally, in the present work we show (*vide infra*) that a third pathway where a hydride transfer process leads to a cationic alkyl intermediate

(R^+) and a bishydroxo $\text{Fe}^{\text{III}}(\text{OH})_2(\text{L})$ unit (C) cannot be *a priori* discarded. Transfer of one of the hydroxide ligands to R^+ would afford the final hydroxylated product (path c in Scheme 2). This third option is similar to the proposed mechanism for the cyclohexane chlorination by $[\text{Fe}^{\text{V}}(\text{O})(\text{Cl})(\text{TPA})]^{2+}$.³⁰ Therefore, depending on the substrate, catalysts, and method of calculation, several authors arrived at different conclusions about the operative mechanism in AHPs (Scheme 2). A fourth possible mechanism where the substrate radical formed via HAT dissociates and reacts with a second oxo-iron compound to give the corresponding hydroxylated product is also described in literature. This dissociative mechanism has been proposed for the hydroxylation of alkanes catalyzed by $[\text{Fe}^{\text{IV}}(\text{O})(\text{Bn-TPEN})]^{2+}$,³¹ $[\text{Fe}^{\text{IV}}(\text{O})(\text{N4Py})]^{2+}$ ³¹ and $[\text{Fe}^{\text{V}}(\text{O})(\text{TAML})]^-$,^{28,29} and in these three cases this mechanism is supported by theoretical and experimental evidence. Furthermore, Gupta and co-workers suggested that the oxidation of cyclohexane catalyzed by their synthesized biuret-substituted TAML ligand $\text{Fe}^{\text{V}}\text{O}$ compound may proceed by either a rebound mechanism, a dissociative mechanism or a combination of both.²⁸ Then, in principle, it is plausible to propose that dissociation of the substrate radical could be competitive with or preferable to the rebound pathway. However, for the particular case of the $[\text{Fe}^{\text{V}}(\text{O})(\text{OH})(\text{PyTACN})]^{2+}$ compound, all experimental evidences conclusively discard the dissociation mechanism (see below), and thus it has not been studied here.

The main goal of this work is to gain insight into the reaction mechanism of AHPs studying by hydroxylation of methane, ethane, cyclohexane, and 2,3-dimethylbutane (2,3-DMB) catalyzed by the $[\text{Fe}^{\text{V}}(\text{O})(\text{OH})(\text{PyTACN})]^{2+}$ complex (Scheme 1). The studied alkanes were chosen because they bear different types of C–H bonds (methane, primary, secondary, tertiary). Our aim is to investigate whether hydroxylation of C–H bonds of different nature proceeds or not through different reaction pathways. A second goal is to analyze how solvent affects the reaction mechanism of AHPs. To this end, we performed calculations (i) at gas phase, (ii) at gas phase including single-point energy corrections for dispersion and acetonitrile solvent effects, and (iii) in acetonitrile solution (see Computational Details section for more details). The final goal of this study is to identify the key steps of the AHP mechanism to get a better understanding of these reactions that ultimately should help the design of more efficient catalysts.

II. COMPUTATIONAL DETAILS

All values presented in this computational study have been obtained with the Gaussian 09 software package³³ using the spin-unrestricted UB3LYP^{34,35} hybrid DFT functional in conjunction with the SDD basis set and the associated effective core potential (ECP) for Fe ³⁶ and the 6-311G(d,p) basis set for the rest of the atoms. All geometry optimizations were performed without symmetry constraints. Analytical Hessians were

computed to determine the nature of stationary points (one and zero imaginary frequencies for transition states and minima, respectively). Furthermore, the connectivity between stationary points was unambiguously established by intrinsic reaction path calculations.^{37,38}

All final reported energy values were systematically corrected after geometry optimization by removing spin-contamination using the following expressions:^{39,40}

$$E_{\text{spin-corr}} = \frac{E_S - a \cdot E_{(S+1)}}{1 - a} \quad (1)$$

$$a = \frac{\langle S_S^2 \rangle - S \cdot (S + 1)}{\langle S_{(S+1)}^2 \rangle - S \cdot (S + 1)} \quad (2)$$

where E_S and $\langle S_S^2 \rangle$ are the UB3LYP/6-311G(d,p)~SDD electronic energy and square total spin angular momentum of the S spin state obtained by means of an unrestricted calculation. $E_{(S+1)}$ and $\langle S_{(S+1)}^2 \rangle$ are the electronic energy and square total spin angular momentum obtained for the $(S+1)$ spin state computed with the same level of theory and at the geometry of the S spin state. $E_{\text{spin-corr}}$ is the spin-corrected electronic energy.

From this general level of theory, three different computational methodologies were used. First, we calculated relative gas-phase Gibbs energy values (ΔG_g) including spin-corrected UB3LYP/6-311G(d,p)~SDD electronic energies ($E_{\text{spin-corr}}^g$), together with thermal and entropy corrections at 298.15 K obtained from frequency calculations (G_{corr}^g) (eq 3). Second, we obtained relative Gibbs energies ($\Delta G_{g+\text{corr}}$) that included relative gas-phase Gibbs energy values plus single-point Gibbs solvation energies in acetonitrile solution ($G_{\text{solv-corr}}^g$) and dispersion corrections (E_{disp}^g) (eq 4). Dispersion effects were calculated using the Grimme DFT-D2 method,⁴¹ whereas solvation effects were computed using the Polarizable Continuum Model–SMD method developed by Truhlar and co-workers, which is based on the quantum mechanical charge density of the solute molecule interacting with a continuum description of the solvent.⁴² The solvent contribution was obtained as the difference between the electronic energy at gas phase and in solution both computed with the B3LYP method and the 6-31G(d) basis set, the basis set used to parametrize the SMD method. All calculated solvation Gibbs energies use a standard state of an ideal gas at a gas-phase concentration of 1 mol/L dissolved as an ideal dilute solution at a liquid-phase concentration of 1 mol/L. The change of conventional 1 atm standard state for gas-phase calculations to a standard-state gas-phase concentration of 1 M requires the introduction of a concentration-change term of 1.89 kcal/mol at 298.15 K, $\Delta G^{o/*}$. Finally, in the third computational methodology used (ΔG_{solv}), the effect of the acetonitrile solution and the D2 dispersion corrections were taken into account during geometry optimization processes at the UB3LYP/6-311G(d,p)~SDD level of theory ($E_{\text{spin-corr}}^{\text{solv}} + E_{\text{disp}}^{\text{solv}} + G_{\text{solv-corr}}^{\text{solv}}$), instead of being added through single-point energy calculations at the gas-phase optimized geometries (eq 5). Then, following the approach suggested by Cramer et al., Gibbs energy corrections at 298.15 K obtained from frequency calculations at the solvent-phase optimized geometries ($G_{\text{corr}}^{\text{solv}}$) were added.⁴³ We can summarize the energy contributions included in each approach as follows:

$$G_g = E_{\text{spin-corr}}^g + G_{\text{corr}}^g \quad (3)$$

$$G_{g+\text{corr}} = E_{\text{spin-corr}}^g + E_{\text{disp}}^g + G_{\text{solv-corr}}^g + G_{\text{corr}}^g + \Delta G^{o/*} \quad (4)$$

$$G_{\text{solv}} = E_{\text{spin-corr}}^{\text{solv}} + E_{\text{disp}}^{\text{solv}} + G_{\text{solv-corr}}^{\text{solv}} + G_{\text{corr}}^{\text{solv}} + \Delta G^{o/*} \quad (5)$$

Unless otherwise noted, energies discussed in this work were obtained using eq 5. In the Supporting Information (SI), we provide tables with energies obtained using eqs 3 and 4.

The rigorous accurate computational study of electron-transfer (ET) processes in solvent requires expensive multiconfigurational calculations in order to describe electronic states properly. Moreover, the search of the ET barrier in solution, at UB3LYP/SMD level of theory, did not yield a good description of the barrier. UB3LYP/SMD led to abrupt

changes in the potential energy surfaces instead of a smooth description of the ET potential energy profile even when the more flexible IEFPCM model was used.⁴⁴ In this work, to compute the ET barriers, we used the widely accepted classical Marcus formalism.^{45,46} The Marcus theory uses the Gibbs energy of the redox reaction ($\Delta G^o = \Delta G_{\text{prod}} - \Delta G_{\text{react}}$) and the reorganization energy (λ) to calculate the ET Gibbs energy barrier (ΔG^*) through

$$\Delta G^* = \frac{(\Delta G^o + \lambda)^2}{4\lambda} \quad (6)$$

The reorganization energy (λ) is the energy change due to the whole chemical system (the complex and the surrounding solvent molecules) rearrangement. It splits into inner-sphere reorganization energies, λ_{isr} , and outer-sphere reorganization energies, λ_{os} ($\lambda = \lambda_{\text{isr}} + \lambda_{\text{os}}$). λ_{is} is the relaxation energies for the complex, while λ_{os} accounts for the required energy to reorganize solvent distribution surrounding the complex. λ_{is} has the precursor contribution, λ_{is1} , and the products contribution, λ_{is2} ($\lambda_{\text{is}} = \lambda_{\text{is1}} + \lambda_{\text{is2}}$). λ_{is1} is the difference between the energy of products in their ground state at the precursors geometry, $E(\text{Prod})_{\text{PRE}}$, and the energy of products at their ground state optimized geometry, $E(\text{Prod})_{\text{OPT}}$ (eq 7). Similarly, λ_{is2} is the difference between the energy of precursors in their ground state at the products geometry, $E(\text{Pre})_{\text{PROD}}$, and the energy of precursors at their ground state optimized geometry, $E(\text{Pre})_{\text{OPT}}$ (eq 8) (see Figure 1).

$$\lambda_{\text{is1}} = E(\text{Prod})_{\text{PRE}} - E(\text{Prod})_{\text{OPT}} \quad (7)$$

$$\lambda_{\text{is2}} = E(\text{Pre})_{\text{PROD}} - E(\text{Pre})_{\text{OPT}} \quad (8)$$

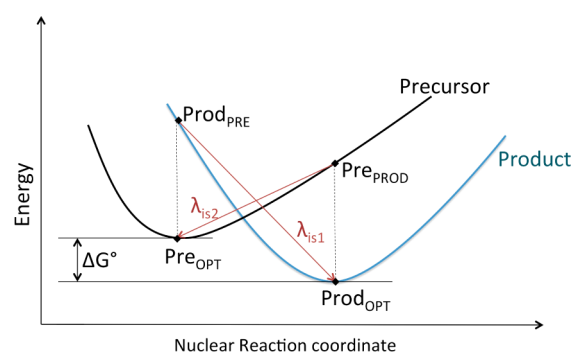


Figure 1. Schematic illustration of the procedure used for the calculation of inner-sphere reorganization energies (λ_{is}).




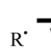

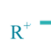

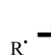

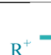
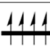
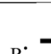
Meanwhile, the λ_{os} for continuum solvent models is given by

$$\lambda_{\text{os}} = (\Delta q)^2 \left(\frac{1}{2r_1} + \frac{1}{2r_2} - \frac{1}{R} \right) \left(\frac{1}{D_{\text{op}}} - \frac{1}{\epsilon_s} \right) \quad (9)$$

where Δq is the charge transferred, r_1 and r_2 are the effective radii of the precursor molecules, R is the effective radius of the whole precursor complex, and ϵ_s and D_{op} are the static and high-frequency (optical) dielectric constants of the solvent. Radii are expressed in angstroms and, in our case, the charge transferred is equal to 1, and ϵ_s and D_{op} for acetonitrile are 35.688 and 1.801, respectively. The final λ_{os} value is given in eV.



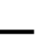
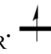
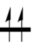
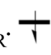



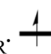
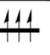
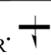


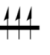
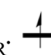
The self-interaction error (SIE) intrinsic in density-functional theory has also been taken into account. SIE in DFT is the consequence of the fact that the residual self-repulsion in the Coulombic term of the energy functional is not totally canceled by the exchange part of the functional.^{47,48} The SIE artificially stabilizes delocalized states, since delocalization reduces the self-repulsion.⁴⁹ Siegbahn et al. proposed a simple approach to measure the magnitude of the SIE effects in systems composed of a catalytic transition metal complex and a substrate molecule.⁵⁰ Their approach is based on the comparison of electronic spin density and energy of *a priori* two quasi-equivalent DFT structures: (i) the localized states of the catalyst and substrate at infinite distance

Table 1. Relative Gibbs Energies (ΔG_{solv} in kcal/mol) for Radical and Cation Iron-Bishydroxo Catalyst Intermediates for Different Spin Multiplicities

UB3LYP-D2-SMD			substrates / ΔG_{solv} (kcal/mol)				
S	electronic configuration		methane	ethane	cyclohexane	2,3-DMB	
	iron	substrate					
1/2	I_{cat}	C 	R ⁺ 	- ^a	9.66	10.38	- ^a
	I_{rad}	B 	R [•] 	0.00	8.86	23.28	- ^a
3/2	I_{cat}	C 	R ⁺ 	- ^a	9.34	9.52	10.52
	I_{rad}	B 	R [•] 	1.12	9.75	22.70	34.55
5/2	I_{cat}	C 	R ⁺ 	- ^a	0.00	0.00	0.00
	I_{rad}	B 	R [•] 	6.55	- ^a	- ^a	- ^a

^aWe were unable to optimize the intermediate in this particular electronic configuration. Key symbols: B = Fe^{IV}(OH)₂; R[•] = radical substrate; I_{rad} = B/R[•]; C = Fe^{III}(OH)₂; R⁺ = cationic substrate; I_{cat} = C/R⁺.

Table 2. Relative Gibbs Energies (ΔG_{solv} in kcal/mol) for Several Radical and Cation Iron-Bishydroxo Catalyst Electronic Configurations, Evaluated Considering Catalyst and Substrate Separated at Infinite Distance^a

UB3LYP-D2-SMD			substrates / ΔG_{solv} (kcal/mol)				
S	iron configuration	substrate configuration	methane	ethane	cyclohexane	2,3-DMB	
1/2	I_{cat}	C 	R ⁺ 	26.65 (26.65)	10.37 (0.00)	10.37 (0.00)	10.37 (0.00)
	I_{rad}	B 	R [•] 	11.85 (11.85)	25.02 (14.64)	37.81 (27.43)	48.89 (38.51)
	I_{rad}	B 	R [•] 	0.00 (0.00)	13.16 (2.79)	25.95 (15.58)	37.03 (26.66)
3/2	I_{cat}	C 	R ⁺ 	26.61 (26.61)	10.34 (0.00)	10.34 (0.00)	10.34 (0.00)
	I_{rad}	B 	R [•] 	0.00 (0.00)	13.16 (2.83)	25.95 (15.62)	37.03 (26.70)
	I_{rad}	B 	R [•] 	5.66 (5.66)	18.82 (8.49)	31.61 (21.28)	42.70 (32.36)
5/2	I_{cat}	C 	R ⁺ 	16.27 (10.61)	0.00 (0.00)	0.00 (0.00)	0.00 (0.00)
	I_{rad}	B 	R [•] 	5.66 (0.00)	18.82 (18.82)	31.61 (31.61)	42.70 (42.70)

^aValues in parentheses correspond to Gibbs energy differences within the same multiplicity species. Key symbols: B = Fe^{IV}(OH)₂; R[•] = radical substrate; I_{rad} = B/R[•]; C = Fe^{III}(OH)₂; R⁺ = cationic substrate; I_{cat} = C/R⁺.

obtained from two different calculations, and (ii) the states obtained from a single calculation of the catalyst and substrate separated by a very long distance (e.g., 60 Å). The only difference between both types of calculations should be the small Coulomb interaction between the catalyst and the substrate at 60 Å. If the latter DFT calculation leads to different electronic spin density and lower energy than the former (after

removing the effect of the Coulomb interaction), the DFT calculation of such catalyst–substrate complex suffers SIE effects. On the contrary, if both calculations lead to the same electronic spin density and energy, there is no evidence of SIE effects on the catalyst–substrate complex. In this paper we have used this approach to measure the possible SIE effects of the compounds studied here (see SI for more details).

The AHP may involve different spin states. In our work, we have analyzed the doublet, quartet, and sextuplet potential energy surfaces (PESs). Superscripts in the labels of the different species along the reaction coordinate refer to their spin multiplicity; 2, 4, and 6 stand for doublet, quartet, and sextuplet, respectively. The relative spin state energies of UB3LYP/6-311G(d,p)~SDD structures have been checked at UOPBE/6-311G(d,p)~SDD level of theory (see Tables S4 and S5). Previous validation studies have shown the validity of the OPBE functional for the spin-state splittings of iron complexes.^{51–54} The comparison between UB3LYP and UOPBE spin ground states indicates that same qualitative pictures are obtained with the two functionals. The same conclusion was drawn by de Visser et al. when comparing the spin state splittings obtained using the UB3LYP, UBLYP, UB3PW91, and TPSS functionals.⁵⁵ For this reason, we will focus on the UB3LYP results only.

For the cases where the energy surfaces of two spin multiplicities were close in energy and the obtained spin crossing was reliable, the minimum energy crossing points (MECPs) were optimized and evaluated using Gaussian 09 together with the code developed by Harvey et al.⁵⁶

III. RESULTS AND DISCUSSION

1. Electronic Structure and Stability of the Iron-Bishydroxo Intermediate (B or C) Formed after C–H Bond Breakage. The main difference between all pathways suggested in Scheme 2 lies on the stability and the electronic structure of the intermediate species that are formed after substrate C–H breakage by the $\text{Fe}^{\text{V}}(\text{O})(\text{OH})$ species (A): $\text{B}/\text{R}^{\bullet}$ (I_{rad}) or C/R^+ (I_{cat}). As explained above the examples reported in the literature suggest either (i) a highly asynchronous concerted mechanism for alkane hydroxylation (path b in Scheme 2) without the existence of an intermediate or (ii) the rebound mechanism through a $\text{R}^{\bullet}/\text{B}$ intermediate (path a in Scheme 2). Nevertheless, in this work several R^+/ C intermediates have been optimized using different theoretical models. Furthermore, in most of the cases they are even thermodynamically more stable than their I_{rad} counterparts. These results suggest that the third pathway, labeled as path c in Scheme 2, may be also possible.

Table 1 summarizes the relative ΔG_{solv} stabilities of I_{rad} and I_{cat} intermediates at the three different spin states studied and for all analyzed substrates, namely, methane, ethane, cyclohexane, and 2,3-DMB. For each total spin state and iron oxidation state, only the most stable electronic configuration has been studied. The results show that the relative stability of methane intermediates is clearly different from that of other substrates. Most stable methane intermediates have the $\text{R}^{\bullet}/\text{B}$ electronic structure for each of the three spin multiplicities studied. Indeed the methyl cation/C form could not be optimized. On the contrary, for all other substrates, the most stable iron-bishydroxo structure is R^+/C . The $\text{I}_{\text{rad}} - \text{I}_{\text{cat}}$ energy difference linearly correlates with the ionization energies (IE) of the substrate (see Figures S9 and S10), which can be used to predict the relative stability of the two intermediates. Obviously, the correlation is even better if the IE of substrates are replaced by the IE of the alkyl radicals (see Figure S8 and below for further discussion).

Table 2 lists the relative ΔG_{solv} stabilities of I_{rad} and I_{cat} intermediates when considering the substrate and the catalyst separated by an infinite distance. Thus, it presents the relative Gibbs energies of all possible combinations between the radical with $S = 1/2$ (cationic with $S = 0$) substrate and the $S = 0$, $S = 1$, and $S = 2$ spin states of the B species ($S = 1/2$, $S = 3/2$, and $S = 5/2$ spin states of the C species). Only the most stable I_{rad} combinations shown in Table 2 were optimized as I_{rad} intermediates (Table 1). In agreement with the results in Table 1, the data presented in Table 2 indicates that while methane has an I_{rad} form as the lowest energy state, for all other

substrates the I_{cat} represents the lowest energy structure. The simple model used in Table 2 does not take into account the coupling between the substrate and the iron species. However, the approximate values of Table 2 are useful to offer an explanation on the relative Gibbs energies for the different intermediates at the different spin states. For instance, the results of Table 2 for methane point out that for $S = 1/2$ the lowest-lying electronic state corresponds to the antiferromagnetic coupling of the methyl radical and the $S = 1$ B species, whereas the methyl radical/ $S = 0$ B or methyl cation/ $S = 1/2$ C electronic states are more than 10 kcal/mol higher in energy.

Tables 1 and 2 show that for I_{cat} species the most stable multiplicity is always sextuplet, while for I_{rad} intermediates the lowest-lying energy structures involve always a $S = 1$ B moiety. For the latter, energies between antiferromagnetic and ferromagnetic equivalent species have always close values indicating a weak spin coupling between the unpaired electrons of the two fragments (see I_{rad} species with total spin equals to $S = 1/2$ and $S = 3/2$ in Table 1). With the exception of methane, the most stable intermediate is I_{cat} in sextuplet multiplicity, due in part to the extra stability given by the half-filled d shell of the iron center. On the contrary, geometry optimization of the sextuplet radical states, which are given by a ferromagnetic coupling between R^{\bullet} and the $S = 2$ B catalyst, yields directly to alcohol products without the presence of a stable intermediate. Furthermore, results of Table 2 indicate that the doublet and quadruplet I_{rad} are for all the substrates more stable than the sextuplet.

As a general trend, I_{cat} stabilization with respect to its I_{rad} counterpart ($\Delta G_{\text{solv}}^{\text{I}_{\text{rad}}} - \Delta G_{\text{solv}}^{\text{I}_{\text{cat}}}$) increases when the number of carbons attached to the carbon that suffers the HAT increases (see Table 2). Thus, the sextuplet cationic ethyl, cyclohexyl, and 2,3-DMB/B intermediates are, respectively, 13.2, 26.0, and 37.0 kcal/mol more stable than the lowest energy I_{rad} intermediates, while for methane, I_{rad} is favored over cationic methyl/B by 16.3 kcal/mol. This can be easily predicted just from the ionization energy of R^{\bullet} (IE_{subst}) and the electron affinity of the B moiety (EA_{cat}) (see Tables S1 and S2). For all the studied substrates but methane the ET process is thermodynamically favorable in solution (i.e., $\text{IE}_{\text{subst}} - \text{EA}_{\text{cat}} < 0$).

In summary, the results obtained analyzing all possible electronic states of the intermediates indicate that the new proposed mechanism c of Scheme 2 could be the most favorable for C–H oxidation at primary, secondary, or tertiary carbon atoms.

2. Mechanistic Study of the Alkane Hydroxylation Process (AHP). *2.a. Hydrogen Atom Transfer (HAT) Process.* $[\text{Fe}^{\text{V}}(\text{O})(\text{OH})(\text{PyTACN})]^{2+}$ has been proposed as the active species in alkane^{22–24} and water^{57–59} oxidation. Moreover, its generation and its reaction with olefins has been proved by variable-temperature mass spectroscopy and DFT calculations.⁶⁰ The *cis* relative disposition of the oxo and hydroxo ligands gives two possible isomeric forms for $[\text{Fe}^{\text{V}}(\text{O})(\text{OH})(\text{PyTACN})]^{2+}$. The $[\text{Fe}^{\text{V}}(\text{O})(\text{OH})(\text{PyTACN})]^{2+}$ isomeric form that has the oxo group *trans* to a N–CH₃ moiety of the PyTACN ligand is the most stable one,²³ and consequently in the present mechanistic study it is assumed as the initial active species, A. To identify the key steps for the AHP, in this section we study the first step of the process, that is, the HAT process for all the studied substrates in acetonitrile solution (see Scheme 2).

An alternative to the HAT for the first step of the mechanism is a long-range electron transfer from the substrate to the high-valent $[\text{Fe}^{\text{V}}(\text{O})(\text{OH})(\text{PyTACN})]^{2+}$. This ET first step mecha-

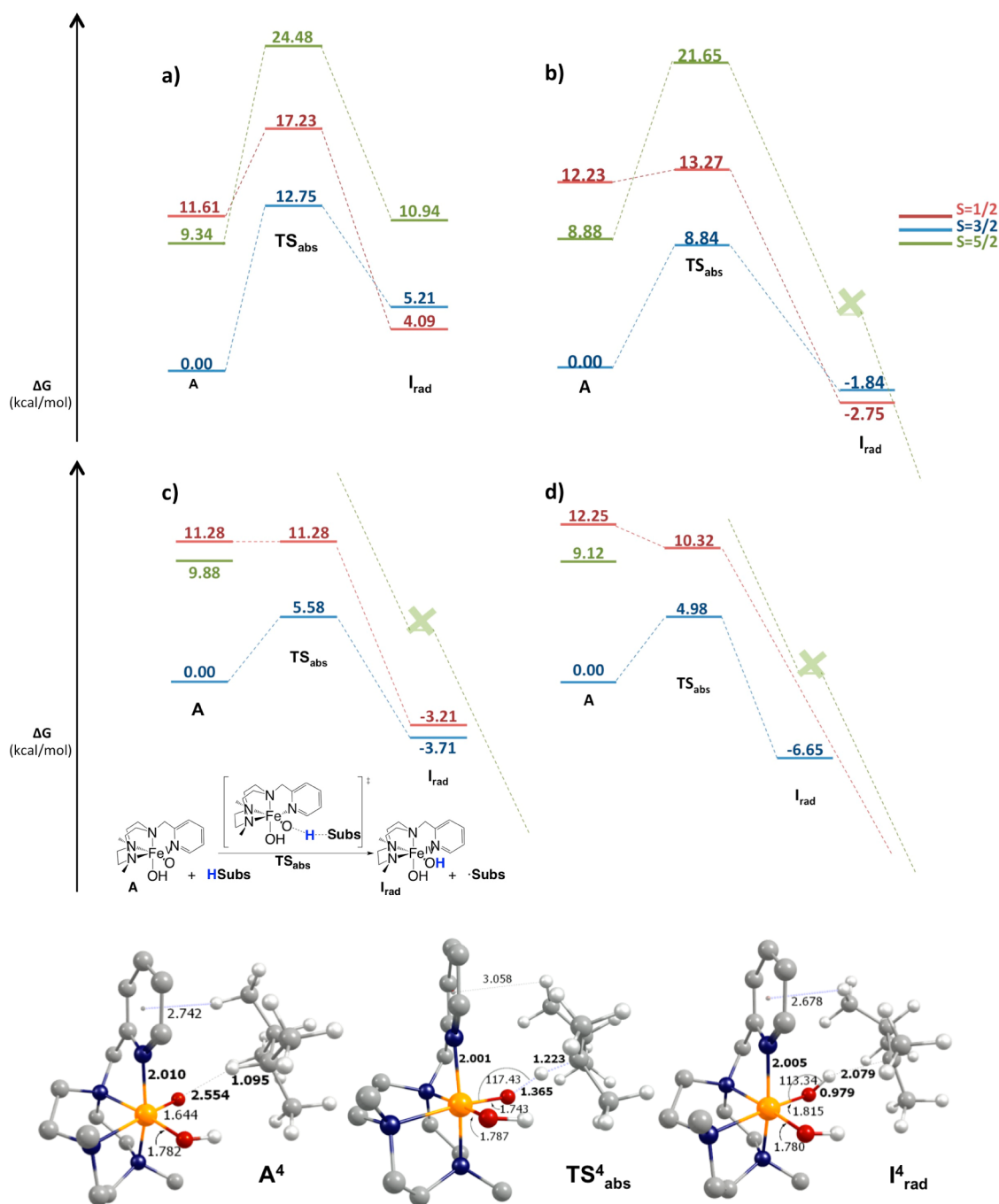


Figure 2. (Top) Gibbs energy profiles in solution (ΔG_{soln}) of the HAT step for (a) methane, (b) ethane, (c) cyclohexane, and (d) 2,3-DMB (kcal/mol). Red, blue, and green profiles correspond to doublet, quartet, and sextuplet multiplicities, respectively. (Bottom) Structures of the HAT process for 2,3-DMB substrate in the ground state ($S = 3/2$). Selected distances and angles are indicated in angstroms (Å) and in degrees (deg), respectively. C atoms are represented in gray, N in blue, O in red, Fe in orange, and H in white. Hydrogen atoms of the PyTACN ligand have been omitted for clarity.

nism was computationally determined by de Visser et al. as the most viable for $[\text{Fe}(\text{O})(\text{BQEN})(\text{NCCH}_3)]^{3+}$ (BQEN = *N,N'*-dimethyl-*N,N'*-bis(8-quinolyl)ethane-1,2-diamine), an iron(IV)-oxo ligand cation radical which has an extremely large electron affinity.⁶¹ The same charge transfer first step mechanism was also proposed on the basis of computational studies for Cpd I of P450⁶² and non-heme iron(IV)-tosylimido species.⁶³ However, for $[\text{Fe}^{\text{V}}(\text{O})(\text{OH})(\text{PyTACN})]^{2+}$ the ET is always far more endothermic than the HAT barrier, so that the ET mechanism can be clearly ruled out (see Tables S7 and S8).

The Gibbs energy profiles for the HAT step of the four studied substrates are presented in Figure 2. The ground state of the initial active $\text{Fe}^{\text{V}}(\text{O})(\text{OH})$ species (A^4) and HAT transition states (TS_{abs}^4) are quartet spin states for all substrates, while $S = 1/2$ and $S = 5/2$ excited spin states are, at least, 4.5 kcal/mol higher in energy. The first excited state of $\text{Fe}^{\text{V}}(\text{O})(\text{OH})$ species is the sextuplet state and the second has a doublet spin state configuration. However, the opposite is true for the TS of the hydrogen abstraction. The inclusion of spin contamination, thermal, and entropy corrections have a key effect on the relative energy of the different spin states of the intermediates and

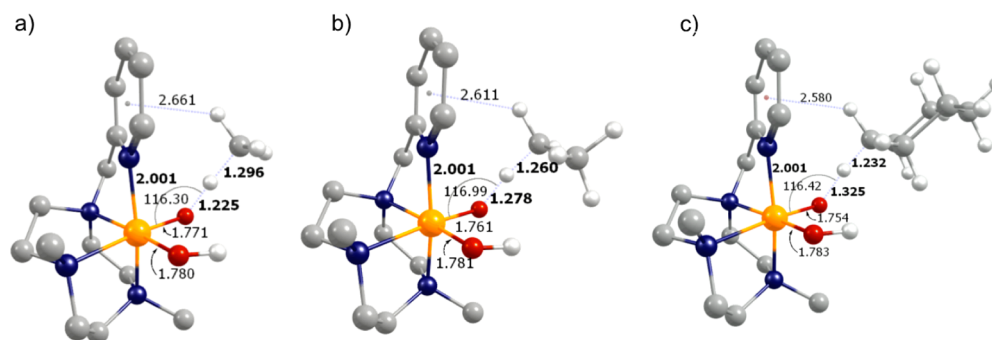
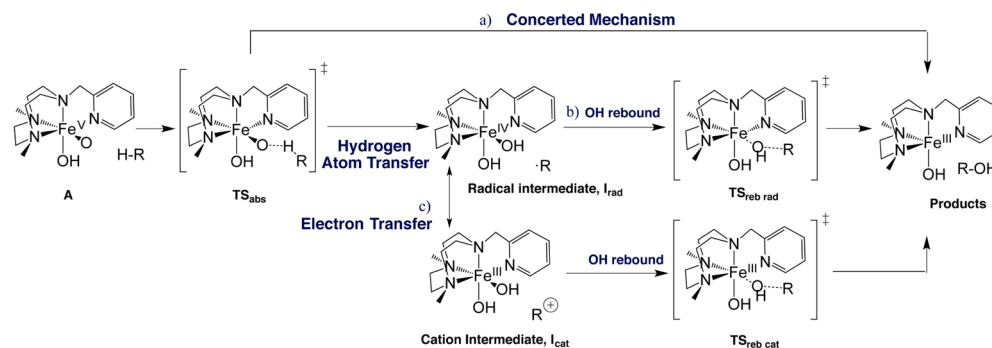


Figure 3. TS_{abs} structures in solution at $S = 3/2$ for (a) methane, (b) ethane, and (c) cyclohexane, TS_{abs}⁴. Distances in Å and angles in degrees. C atoms are represented in gray, N in blue, O in red, Fe in orange, and H in white. Hydrogen atoms of the PyTACN ligand have been omitted for clarity.

Scheme 3. Three Proposed Mechanisms for Alkane Hydroxylation Processes Catalyzed by [Fe^V(O)(OH)(PyTACN)]²⁺



transition states species (see Table S4). For cyclohexane, the calculated kinetic isotopic effect (KIE) for TS_{abs}⁴ using the classical transition state theory expressions is 4.9, in very good agreement with the experimental KIE = 4.3.²³

Spin population analysis of A² and A⁴ reveals two unpaired electrons on the iron and one unpaired electron on the oxo ligand antiferromagnetically or ferromagnetically coupled, respectively (see Table S3). The presence of this antiferromagnetic coupling translates into an important spin contamination correction in the unrestricted calculation of A⁶. The electronic distribution for A⁶ is clearly different and shows three unpaired electrons on iron, a partial unpaired electron on the oxo ligand and almost an unpaired electron centered on the nitrogen atom of the pyridine group.

Our results show that HAT Gibbs energy barriers (ΔG^\ddagger) decrease when the number of carbon atoms bound to the C–H group that suffers the hydrogen abstraction increases. The same trend is found for the Gibbs reaction energies (ΔG_{reac}). $\Delta G_{\text{A} \rightarrow \text{I}_{\text{rad}}}$ becomes more exergonic when the number of carbons bound to the C that suffers hydrogen abstraction increases. Then, whereas the HAT step for methane is endergonic (4.1 kcal/mol), for ethane, cyclohexane, and 2,3-DMB, the HAT process is exergonic by -2.8 , -3.7 , and -6.7 kcal/mol, respectively. And in agreement with the Bell–Evans–Polanyi principle, the hydrogen abstraction Gibbs energy barrier evolves from 12.8 kcal/mol for methane to 8.8, 5.6, and 5.0 kcal/mol for ethane, cyclohexane, and 2,3-DMB, respectively. Moreover, the HAT Gibbs energy barriers (ΔG^\ddagger) also concur with the strength of the broken C–H bond: the highest ΔG^\ddagger for the strongest C–H bond of methane, and then a lower ΔG^\ddagger for ethane, cyclohexane, and 2,3-DMB, respectively. The binding dissociation energy of the C–H bond is in part determined by the free radical stability that follows the order methyl < primary < secondary < tertiary.⁶⁴

As it was previously shown by de Visser et al.,^{65–67} the HAT energy barriers of the different substrates correlates linearly with the C–H bond dissociation energy ($\text{BDE}_{\text{C-H}}$) of the substrate abstracted hydrogen (see Figures S6 and S7). Furthermore, the HAT energy barriers also show a good linear correlation with IEs of the substrates (see Figure S5). The larger the IE, the higher the HAT barrier.

In addition, our calculations also show a clear relation between the HAT energy barrier and the TS_{abs} geometric parameters (see Figure 3 and Table S5). The longer (shorter) the C–H (O–H) bond distance in the TS_{abs}, the higher the HAT Gibbs energy barrier, thus suggesting a “late” transition state for higher barriers, in agreement with the predictions of the Hammond postulate. Hence, methane has the largest C–H distance and the shortest H–O distance for TS_{abs} structures (late transition state), whereas 2,3-DMB has the shortest C–H distance and the largest H–O distance among the different TS_{abs} structures. The HAT barrier shows very good linear correlations with respect to the O–H bond distance and C–H bond distance of the TS_{abs} structures (see Figures S1 and S2). Furthermore, as it is shown in Figures S3 and S4, the HAT barriers also correlate with the imaginary frequencies and the spin density of the C bonded to the abstracted hydrogen of the TS_{abs}. The HAT barrier increases when the absolute values of the imaginary frequency and C spin density increase. A high value of the C spin density indicates a late HAT transition state.

TS_{abs} structures present a Fe–O–H angle of 108–117° for all studied multiplicities and substrates (see Figure 3). Thus, following Solomon and Neese terminology,^{68,69} the reaction proceeds via a π -channel with an orientation of the substrate that enhances the orbital overlap without increasing too much the Pauli repulsion. Although we have also searched the linear σ -channel HAT transition state for the quadruplet and sextuplet

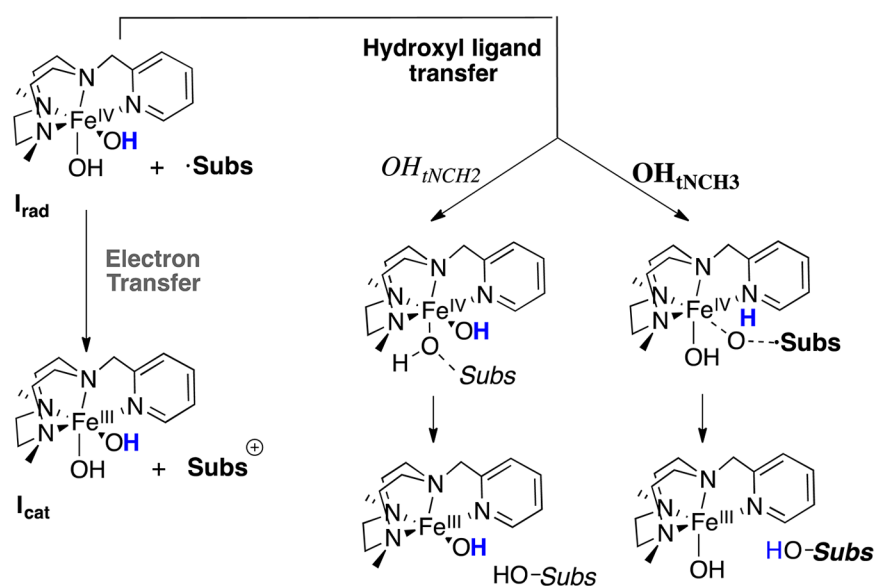
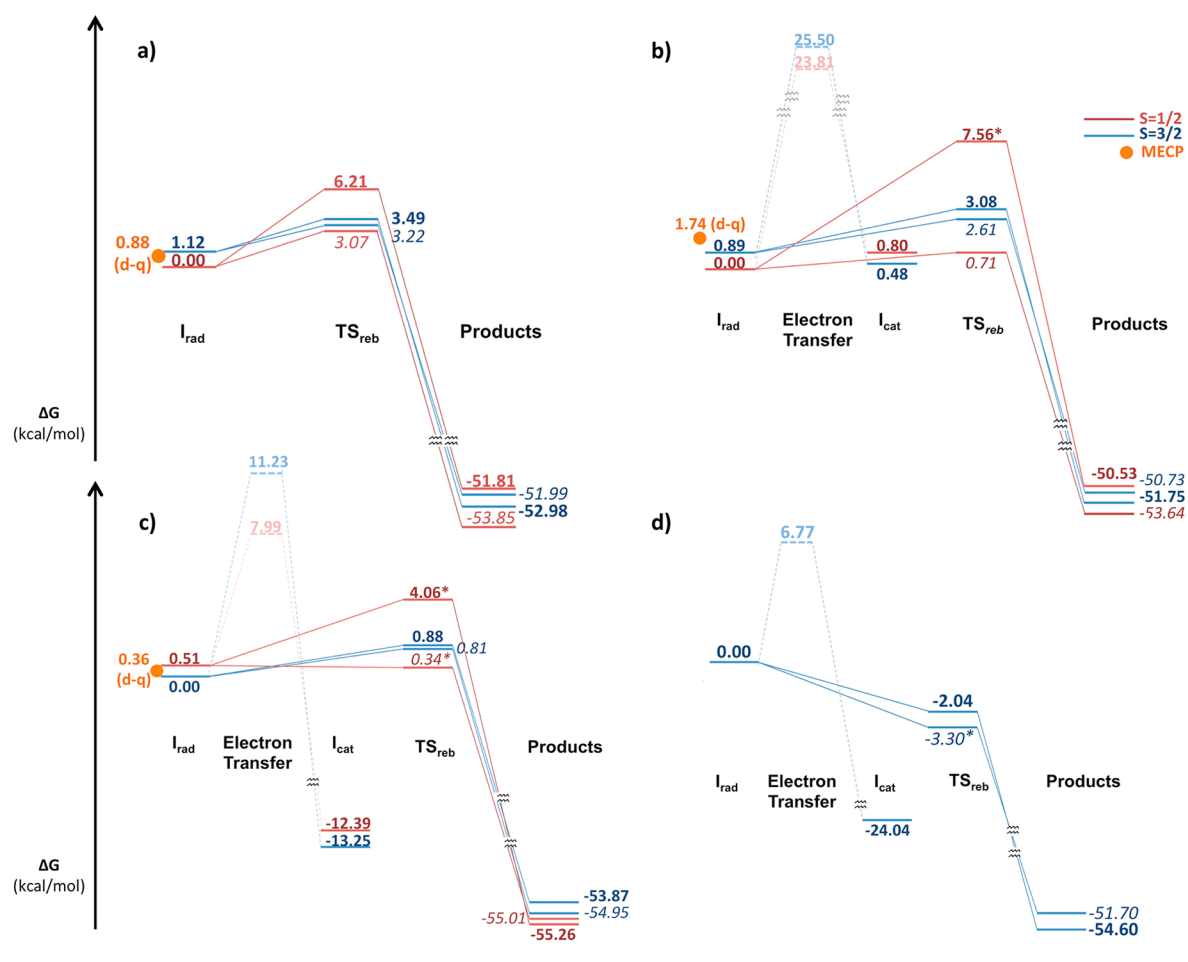


Figure 4. (Top) Gibbs energy profiles (in kcal/mol) in acetonitrile solution (ΔG_{soln}) of the ET and the hydroxyl ligand transfer for (a) methane, (b) ethane, (c) cyclohexane, and (d) 2,3-DMB catalyzed by $[Fe^{IV}(OH)(OH)(PyTACN)]^{2+}$. Red profiles correspond to doublet and blue ones to quartet multiplicity states. Values in *italics* represent the OH_{tNCH_2} ligand transfer, and **bold** values represent the OH_{tNCH_3} ligand transfer. The values marked with an * are approximated upper bound solutions obtained by scanning the C–O bond in linear transits from I_{rad} to products. (Bottom) Reaction mechanisms analyzed in the Gibbs energy profiles.

states, all optimizations lead to the angular π -channel for the TS of the hydrogen abstraction. This scenario is in contrast with HAT reactions by $S = 1$ $Fe^{IV}O$ complexes, that can occur both via

σ - and π -paths.⁷⁰ The presence of a CH/π interaction⁷¹ between all substrates and the pyridine ring of $[Fe^V(O)(OH)-$

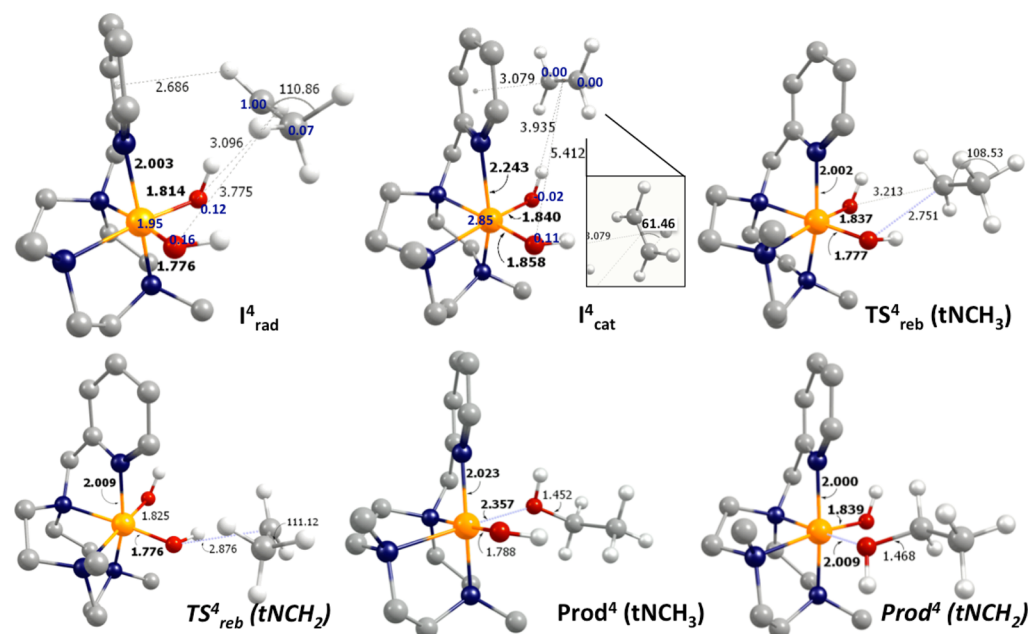


Figure 5. Structures involved in the ET and the hydroxyl ligand transfer processes for ethane. Selected distances and angles are indicated in angstroms (Å) and in degrees (deg), respectively. Selected spin densities (in electrons) are given in blue. C atoms are represented in gray, N in blue, O in red, Fe in orange, and H in white. Hydrogen atoms of the PyTACN ligand have been omitted for clarity.

(PyTACN)]²⁺ complex favors the substrate orientation that triggers the π -channel for the hydrogen abstraction processes.

Intrinsic reaction coordinate (IRC) calculations were done for TS_{abs}^4 in order to ensure connection with the active species A and the next intermediate (I_{rad}^4 or I_{cat}^4). The IRC calculations show that TS_{abs}^4 always leads to an I_{rad}^4 intermediate (see Figure 2). Thus, in acetonitrile solution, the studied hydroxylation reactions at the $S = 3/2$ ground state are stepwise because the HAT does not lead directly to products, but instead an I_{rad}^4 intermediate is found. However, for $S = 5/2$ state of ethane, cyclohexane, and 2,3-DMB and the $S = 1/2$ state for 2,3-DMB, TS_{abs}^4 directly connects with the final products. Thus, for these excited states, the mechanism can be defined as a highly asynchronous concerted process. Although for all the substrates but methane I_{cat}^4 is more stable than I_{rad}^4 , our calculations show that the first step of the mechanism is always hydrogen abstraction instead of a hydride abstraction. Thereby, IRC calculations discard path *c* suggested in Scheme 2. To achieve the more stable I_{cat}^4 , an ET process through a second step would be necessary, and then the proposed mechanisms for AHP for $[\text{Fe}^{\text{V}}(\text{O})(\text{OH})\text{-(PyTACN)}]^{2+}$ could be rewritten as shown in Scheme 3.

2.b. Electron Transfer versus Rebound (Hydroxyl Ligand Transfer). As explained in the previous section, the ground state TS_{abs}^4 always leads to I_{rad}^4 . Nevertheless, after the HAT step, I_{rad}^4 can evolve to the alcohol product through a hydroxyl radical transfer (rebound step path b in Scheme 3) or can be followed by an ET step to I_{cat}^4 (path c in Scheme 3). In this section the competition between the OH radical rebound process and the ET step is evaluated.

The ET step has been studied for the two most stable multiplicities of I_{rad}^4 of ethane and cyclohexane, that is quadruplet and doublet multiplicities. For 2,3-DMB, only quadruplet I_{rad}^4 has been found. For methane I_{cat}^4 is less stable than I_{rad}^4 and the ET was discarded. Marcus theory (see Computational Details) has been used to analyze the kinetics of the ET processes. The kinetics of the hydroxyl radical rebound step was determined by optimizing the corresponding TS. Gibbs energy profiles of the

ET and OH-rebound pathways are shown in Figure 4, and the corresponding structures for the ethane case are depicted in Figure 5.

For A and TS_{abs}^4 , the $S = 3/2$ spin state is the ground state for all substrates. But for I_{rad}^4 , whereas the quadruplet is still the ground state for cyclohexane and 2,3-DMB, for methane and ethane the ground state is $S = 1/2$. The doublet–quadruplet (d–q) minimum-energy crossing point (MECP) for methane, ethane, and cyclohexane I_{rad}^4 intermediates is clearly lower in energy than the quadruplet barriers for the ET and OH-rebound. However, the major change between the doublet and quadruplet spin density is located in the substrate carbon radical, and then the d–q spin-crossing is likely to be not allowed due to the small spin-coupling term of the dipole moment of the transition integral. Nevertheless, we have studied the ET and OH-rebound on doublet and quadruplet multiplicities. Moreover, the TSs for the hydroxyl rebound in the two –OH groups of the $[\text{Fe}^{\text{IV}}(\text{OH})_2(\text{PyTACN})]^{2+}$ structure have also been studied. OH groups are labeled as $\text{OH}_{\text{tNCH}_2}$ and $\text{OH}_{\text{tNCH}_3}$. $\text{OH}_{\text{tNCH}_2}$ is the OH that has an N–(CH₂)₃– group in *trans* (and it is the initial oxo group), whereas $\text{OH}_{\text{tNCH}_3}$ has an N–(CH₂)₂(CH₃)– group in *trans*.

In Figure 4b–d, the ET processes are represented in pale dashed lines, while the two different possible OH-rebounds are represented in bold and italics. For all substrates, Figure 4 clearly shows that the OH-rebound is kinetically more favorable than the ET. For ethane, OH-rebound barriers are between 1.7 and 2.2 kcal/mol, while ET activation energies range from 23.8 to 25.5 kcal/mol. It is worth noting that the C₂H₅⁺ moiety in I_{cat}^4 has the H⁺ bridge C_{2v} conformation, which is the most stable for the free ethyl cation at the B3LYP and CCSD levels of theory (see Figure 5).⁷² For cyclohexane, OH-rebound barriers are in the interval from 0.8 to 0.9 kcal/mol, while ET activation energies are between 8.0 and 11.2 kcal/mol. Finally, 2,3-DMB has a barrierless OH-rebound while the ET process has an energetic cost of 6.8 kcal/mol.

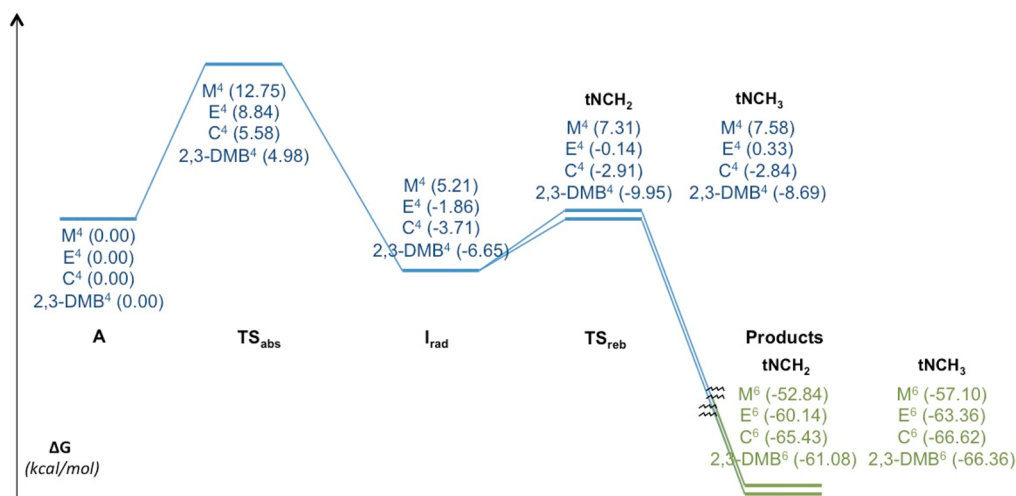


Figure 6. Gibbs energy (in kcal/mol) profiles for methane (M), ethane (E), cyclohexane (C), and 2,3-dimethylbutane (2,3-DMB) hydroxylation processes. Only the ground state for each substrate and structure is represented. Blue accounts for quartet and green for sextuplet ground states.

It has been experimentally proved on the basis of isotopic labeling and product analyses that the radical is short living and does not diffuse freely in the alkane hydroxylation reaction catalyzed by the $[\text{Fe}^{\text{V}}(\text{O})(\text{OH})(\text{PyTACN})]^{2+}$ complex.^{22–24} Therefore, in this paper the dissociation mechanism has not been studied.

To summarize, ET and rebound Gibbs energy barriers share the same behavior: they decrease when the number of C atoms bonded to the radical carbon increases. Indeed both processes account for a $1e^-$ reduction from Fe^{IV} to Fe^{III} and an oxidation of the substrate. The ET is a pure electron transfer, whereas the rebound process entails oxygenation of the substrate to form an alcohol. Thus, in terms of the formal oxidation state of the iron center both reactions formally account for a similar process and share the same behavior (i.e., the barriers decrease from methane to 2,3-DMB), being the barriers for the rebound always lower than the ET barriers.

2.c. The Complete Alkane Hydroxylation Mechanism. From the results obtained in the two previous subsections it can be concluded that (i) AHP always goes through the general *rebound* mechanism (path b in Scheme 2) and (ii) I_{cat} is never an intermediate of the AHP mechanism. The ground state profiles for methane, ethane, cyclohexane, and 2,3-DMB hydroxylation are represented in Figure 6. The ground state of the active initial species, $\text{Fe}^{\text{V}}(\text{O})(\text{OH})$, is always the quartet and the hydrogen abstraction also goes through this multiplicity (which has three unpaired electrons on the catalyst). The Gibbs energy profiles clearly show that the hydrogen abstraction process is the TOF-determining transition state (TDTS).⁷³ I_{rad} $S = 1/2$ and $S = 3/2$ states have similar Gibbs energies for all studied substrates since they have the same electron distribution (three electrons on the catalyst, two in the iron d shell, and one in the oxo moiety) with weak coupling with the substrate (ferromagnetic or antiferromagnetic). Then, I_{rad} ground-state multiplicity varies between $S = 1/2$ and $S = 3/2$ depending on the substrate (doublet for methane and ethane and quartet for cyclohexane and 2,3-DMB) (see Figure 5).

The OH radical rebound (TS_{reb}) has been evaluated for doublet and quartet multiplicities for both isomeric positions despite the d-q spin crossing is likely to be not allowed (see above). The rebound with the OH *trans* to NCH_2 is always the most favorable one and its ground state is again doublet for

methane and ethane and quartet for cyclohexane and DMB, as for I_{rad} (see Figure 5). For quartet spin state, the rebound with the hydroxyl *trans* to NCH_3 is less than 1 kcal/mol higher in energy than the rebound with the OH *trans* to the NCH_2 moiety. Thus, the calculations show that the rebound with the OH *trans* to NCH_2 moiety is the most favorable one, although these results should be taken with some caution since energy differences between both rebounds are within the limits of precision of the used DFT approach. The final products with the alcohol formed fall down to sextuplet states.

3. Comparison between Gas-Phase and Solvent-Phase Mechanisms. As previously mentioned in the introduction, computational studies of the reaction mechanism for alkane oxidation processes catalyzed by $\text{Fe}^{\text{V}}\text{O}$ do not present a clearly established pathway for many substrates and catalysts. DFT equilibrium geometries of the intermediates and transition states of the proposed mechanisms are usually optimized at gas phase. In some cases, the solvent-phase corrections are included through single-point solvent-phase corrections. Here we will show that the single-point calculations approach to include the solvent-phase effects is not always a good method to determine the reaction mechanism in solution and that the solvent effects should also be included during the optimization of the equilibrium geometries. In the first part of this paper, depending on the substrate two different trends for the relative stability of the I_{cat} and I_{rad} intermediates have been observed in solution. While for methane the I_{rad} structure is the most stable, for all the other alkane substrates I_{cat} is the most stable form. To assess the reliability of the different approaches given by eqs 3–5 (i.e., G_{g} , $G_{\text{g+corr}}$, and G_{sol}) to describe AHP properly, one substrate of each group (methane and cyclohexane) has been studied computationally with the three methodologies.

We have also studied the electronic structure and stability of the iron-bishydroxo intermediates for methane and cyclohexane at gas phase (G_{g}) and at gas phase including single-point dispersion and acetonitrile solvent corrections ($G_{\text{g+corr}}$). The gas-phase Gibbs energy of all possible combinations between the radical (cationic) substrate and all possible multiplicities of the catalyst at infinite distance are listed in Tables S6 and S7. Comparison of these gas-phase (Table S6) and solvent-phase (Table 2) values show that the acetonitrile solution stabilizes I_{rad} over the most stable I_{cat} . The larger solvent stabilization of I_{rad} as

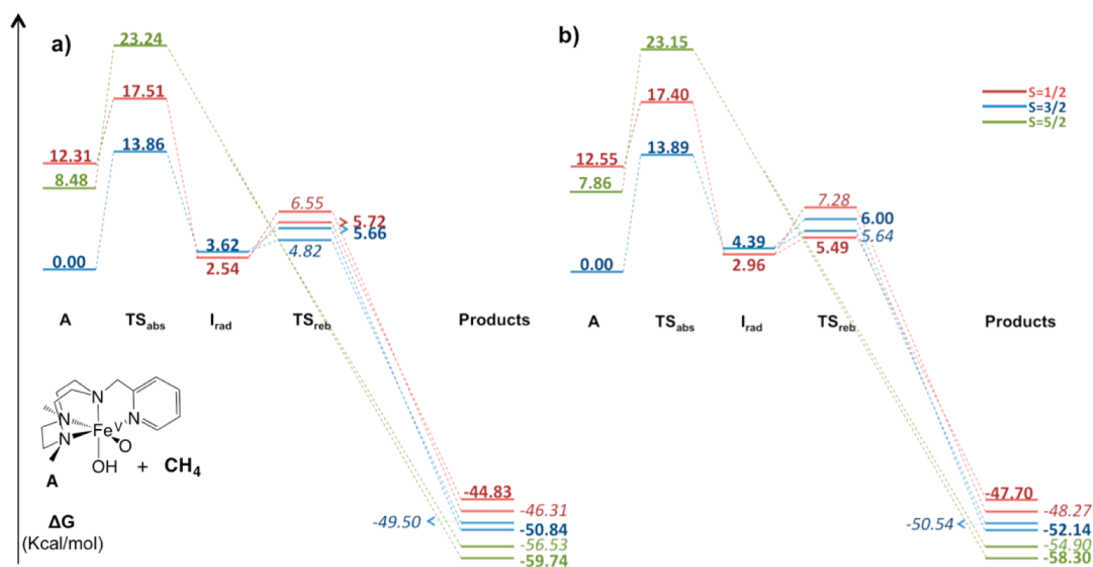


Figure 7. Gibbs energy profile in kcal/mol for the AHP of methane at gas phase (G_g) (a) and at gas phase including the dispersion and solvent corrections (G_{g+corr}) (b). Values in *italics* represent the OH_{tNCH_3} ligand transfer, and **bold** values represent the OH_{tNCH_3} ligand transfer.

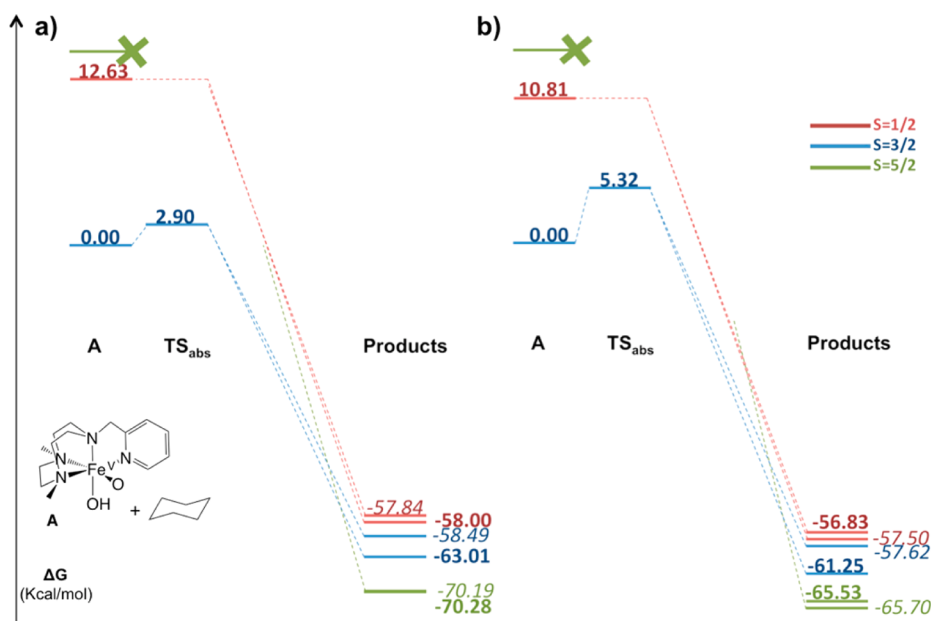


Figure 8. Gibbs energy profiles in kcal/mol for the AHP of cyclohexane at gas phase (a) and at gas phase including dispersion and solvent corrections (b). Values in *italics* represent products where the alcohol group comes from the OH_{tNCH_3} .

compared to I_{cat} is caused by the localization of the +2 positive charge on the catalyst in the former intermediate. The solvent relative stabilization of I_{rad} as compared to I_{cat} increases when the size of the substrate increases. However, the latter effect is smaller than the stabilization of I_{cat} due to the reduction of IE_{subst} when the size of the substrate increases. As it is well-known, the general stability of simple alkyl carbocations follows the trend tertiary > secondary > primary > methyl.⁷⁴ Finally, we want to note that when the single-point energy corrections for dispersion and solvent effects are added to the gas-phase values, the values obtained lead to the same conclusions than the results obtained in solution (see Table S7).

The effect of the coupling between the substrate and the catalyst has also been studied considering the whole intermediate (substrate + catalyst) (see Table S8). Again, gas-phase and

solvent-phase results give the same general trends. However, a few key differences between solvent- and gas-phase intermediates appear here. In the gas phase, unlike in solution, there are no stable I_{cat} (I_{rad}) intermediates for methane (cyclohexane). For these electronic states, optimizations at gas phase lead directly to the alcohol products without finding any stable intermediate. The observed differences already seem to indicate that (i) gas-phase and solution reaction mechanisms can be different for a given substrate and (ii) for two different substrates, the reaction mechanisms can differ even if they are computed in the same phase (gas or solution). This may explain the diversity of alkane hydroxylation reaction mechanisms found in the literature.^{23,25,29,30} For this reason, we studied the gas-phase hydroxylation mechanisms of methane and cyclohexane and we compared them with those obtained in solution.

For methane substrate, the AHP Gibbs energy profile obtained at gas phase (Figure 7) is very similar to the one obtained in solution (Figures 2 and 4) with the exception of the sextuplet multiplicity state, for which the intermediate I_{rad} cannot be optimized at gas phase. Thus, although the $G_{\text{g+corr}}$ approach introduces only part of the solvent effects, for the methane case, $G_{\text{g+corr}}$ methodology gives a good semiquantitative description of the solvent-phase profile.

For cyclohexane, differences between G_{g} , $G_{\text{g+corr}}$ and G_{solv} profiles are qualitatively far more important than for methane. As it has already been mentioned, I_{rad} for cyclohexane at gas phase is not a stable minimum, and after the hydrogen abstraction the process yields directly to products (compare Figure 8 with Figures 2 and 4). The cationic intermediates I_{cat} which are stable minima at gas phase, are not part of the mechanism reaction pathway. Thus, the different stabilization of the intermediates in gas phase and solvent clearly affects the reaction mechanism derived from Gibbs energy profiles. Whereas in solution the cyclohexane hydroxylation by $[\text{Fe}^{\text{V}}(\text{O})(\text{OH})(\text{PyTACN})]^{2+}$ catalyst follows a HAT + rebound stepwise mechanism, at gas phase the cyclohexane hydroxylation mechanism is concerted and highly asynchronous. Nevertheless, in both cases, the TDTS is given by the HAT transition state. In this case, on the contrary to methane hydroxylation, $G_{\text{g+corr}}$ approach turns to be an unreliable method to determine the solvent-phase mechanism.

Another difference between cyclohexane hydroxylation Gibbs energy profiles at gas phase and in solution is that, while at gas phase the $S = 3/2$ products are more stable than $S = 1/2$ products, the opposite is true in solution. Also here $G_{\text{g+corr}}$ approach fails in describing the relative stability of these excited spin states in solution.

Finally, let us mention that in a recent DFT modeling of the C–H abstraction catalyzed by the non-heme $[\text{Fe}^{\text{IV}}(\text{O})(\text{N4Py})]^{2+}$ compound, Shaik et al. showed that for this system the effects of the self-interaction error in DFT lead to an incorrect description of the hydroxylation mechanism.⁷⁵ Using the approach given by Siegbahn,⁵⁰ we have computed the SIE of all optimized radical intermediates, I_{rad} , and cationic intermediates, I_{cat} . Our check covers all substrates and more stable spin states for both gas- and solution-phase optimized structures. None of our optimized structures suffers significant SIE effects (see Tables S13–S18). Nevertheless, Shaik and co-workers' paper and our work are perfectly complementary to describe how to achieve a proper description of the alkane hydroxylation mechanism by means of DFT. In the former case, a $\text{Fe}^{\text{IV}}\text{O}$ species is studied and removing the effects of the SIE is essential. Instead, in our work case, hydroxylation is mediated by a $\text{Fe}^{\text{V}}\text{O}$ species, and SIE has no role. But in both works the utilization of gas-phase optimized structures is strongly discouraged.

IV. CONCLUSIONS

In this work, we have investigated with DFT methods the stereospecific hydroxylation of a series of alkanes (methane, ethane, cyclohexane, and 2,3-dimethylbutane) that occurs in the presence of $[\text{Fe}^{\text{II}}(\text{CH}_3\text{CN})_2(\text{PyTACN})]^{2+}$ species treated with excess H_2O_2 in acetonitrile. Our computational results support the proposal that the mechanism for alkane hydroxylation processes takes place through high-valent $[\text{Fe}^{\text{V}}(\text{O})(\text{OH})(\text{PyTACN})]^{2+}$ species. Furthermore, we have determined the key effects of the substrate and solvent in the hydroxylation mechanism. In acetonitrile solution, a stepwise mechanism that starts with a hydrogen atom transfer and follows with a hydroxyl radical rebound is determined for methane, ethane, cyclohexane,

and 2,3-DMB. The same mechanism is valid for the gas-phase methane hydroxylation. On the contrary, gas-phase cyclohexane hydroxylation evolves through a concerted and highly asynchronous mechanism. Namely, gas-phase I_{rad} intermediates are not stabilized, and the initial HAT yields directly the alcohol products. The differences between acetonitrile solution and gas-phase cyclohexane mechanisms can be attributed to the important stabilization by the acetonitrile solvent of I_{rad} intermediate that has a 2+ charge in the catalyst and is neutral in the R^\bullet moiety.

I_{cat} structures are thermodynamically more stable than I_{rad} intermediates for ethane, cyclohexane, and 2,3-DMB. However, IRC calculations and Marcus theory prove that the I_{cat} species are not involved in the hydroxylation mechanism. Although the ET barriers of the evolution of I_{rad} to I_{cat} are smaller than 26 kcal/mol, OH radical rebound barriers for I_{rad} are always far lower. Thus, after the hydrogen abstraction, the iron-bishydroxo intermediate goes to the alcohol products instead of evolving via an ET process. For methane, I_{rad} structures are more stable than I_{cat} ones, and then the ET process can be ruled out. The kinetics of the HAT step is always energetically more demanding than for the rebound step, the former being the rate-determining step.

In a previous work we showed that, for the non-heme iron catalyst studied in this paper, ^{18}O -labeling experiments gave an equal incorporation of oxygen from water and from peroxide in the final cyclohexanol products.²³ Taking into account that the mechanism in acetonitrile solvent is stepwise, in order to explain these labeling results, the activation barriers of both the HAT and the rebound steps should be very similar for the two *cis* active sites. In our previous work, some of us showed that this condition is fulfilled for the HAT step. The results presented here for cyclohexane substrate show that the hydroxyl rebounds barriers for the two –OH groups are nearly identical ($\Delta\Delta G^\ddagger$ of the hydroxyl ligand transfer between the two –OH groups of cyclohexane is less than 0.1 kcal/mol). Thus, the DFT profile for the hydroxylation of cyclohexane catalyzed by $[\text{Fe}^{\text{V}}(\text{O})(\text{OH})(\text{PyTACN})]^{2+}$ presented here is in agreement with the labeling results measured in our previous study. Furthermore, the clarification of the hydroxylation mechanism in acetonitrile solvent as stepwise is also key for the complete rationalization of the experimental ^{18}O incorporation yields that points to the conclusion that the incorporation of oxygen comes only (or mostly) from water or from the peroxide. In this case, both the HAT and the rebound steps should favor one of the two *cis* labile positions of $[\text{Fe}^{\text{V}}(\text{O})(\text{OH})(\text{PyTACN})]^{2+}$.

Finally, the calculation of minimum-energy crossing points between doublet and quartet potential energy surfaces for methane, ethane, and cyclohexane shows that the two-state reactivity does not play a key role in the HAT step. For I_{rad} , the MECF studies show that the energetic cost of crossing from the quadruplet state to the doublet state is always lower than the energy needed to surmount the barriers of the rebound processes. However, the changes between the I_{rad}^2 and I_{rad}^4 spin densities occur in the radical carbon of the substrate, which implies a low spin–orbit coupling term for the spin-crossing transition integral. Therefore, the rebound process evolves always through the $S = 3/2$ spin state potential energy surface since the spin crossing is likely to be not allowed. For the 2,3-DMB hydroxylation, only the quartet state plays a role, since the doublet Gibbs energy profile mechanism, which is concerted, is always much higher in energy.

■ ASSOCIATED CONTENT

■ Supporting Information

The Supporting Information is available free of charge on the ACS Publications website at DOI: 10.1021/acs.inorgchem.5b00583.

Ionization energies of the radical substrates; electron affinities of the B moiety; Mulliken spin population values of A_n complexes; UOPBE energy values for different spin states; energy values for gas phase and gas phase including the dispersion and solvent corrections for all the possible combinations between the radical (cationic) substrate and all possible multiplicities of the catalyst at infinite distance and also considering the optimized intermediate; and xyz coordinates for all the structures (PDF)

■ AUTHOR INFORMATION

Corresponding Authors

*E-mail: miquel.sola@udg.edu.

*E-mail: miquel.costas@udg.edu.

*E-mail: josepm.luis@udg.edu.

Notes

The authors declare no competing financial interest.

■ ACKNOWLEDGMENTS

This work has been supported by Ministerio de Economía y Competitividad of Spain (Projects CTQ2014-54306-P, CTQ2014-52525-P, and CTQ2012-37420-C02-01, Ramón y Cajal contract to A.C., and grant No. BES-2012-052801 to V.P.), Generalitat de Catalunya (project numbers 2014SGR931, 2014SGR862, Xarxa de Referència en Química Teòrica i Computacional, and ICREA Academia prizes for M.S. and M.C.), the European Commission (ERC-2009-StG-239910 to M.C. and FP7-PEOPLE-2011-CIG-303522 to A.C.), and European Fund for Regional Development (FEDER grant UNGI10-4E-801).

■ REFERENCES

(1) Company, A.; Gómez, L.; Costas, M. In *Alkane C-H Activation by Single-Site Metal Catalysis*; Perez, P. J., Ed.; Springer: Dordrecht, 2013; pp 143–228.

(2) Newhouse, T.; Baran, P. S. *Angew. Chem., Int. Ed.* **2011**, *50*, 3362–3374.

(3) Ortiz De Montellano, P. R. *Chem. Rev.* **2010**, *110*, 932–948.

(4) Kovaleva, E. G.; Lipscomb, J. D. *Nat. Chem. Biol.* **2008**, *4*, 186–193.

(5) Costas, M.; Mehn, M. P.; Jensen, M. P.; Que, L., Jr. *Chem. Rev.* **2004**, *104*, 939–986.

(6) Guengerich, F. P.; Munro, A. W. *J. Biol. Chem.* **2013**, *288*, 17065–17073.

(7) White, M. C. *Science* **2012**, *335*, 807–809.

(8) Costas, M. *Coord. Chem. Rev.* **2011**, *255*, 2912–2932.

(9) Que, L., Jr.; Tolman, W. B. *Nature* **2008**, *455*, 333–340.

(10) Codola, Z.; Lloret-Fillol, J.; Costas, M. *Progress in Inorganic Chemistry*; John Wiley & Sons, Inc.: Hoboken, New Jersey, 2014; Vol. 59, p 447.

(11) Bryliakov, K. P.; Talsi, E. P. *Coord. Chem. Rev.* **2014**, *276*, 73–96.

(12) Ensing, B.; Buda, F.; Blöchl, P.; Baerends, E. J. *Angew. Chem., Int. Ed.* **2001**, *40*, 2893–2895.

(13) Buda, F.; Ensing, B.; Gribnau, M. C.; Baerends, E. J. *Chem. - Eur. J.* **2001**, *7*, 2775–2783.

(14) Ensing, B.; Buda, F.; Baerends, E. J. *J. Phys. Chem. A* **2003**, *107*, 5722–5731.

(15) McDonald, A. R.; Que, L., Jr. *Coord. Chem. Rev.* **2013**, *257*, 414–428.

(16) Nam, W.; Lee, Y.-M.; Fukuzumi, S. *Acc. Chem. Res.* **2014**, *47*, 1146–1154.

(17) Kleespies, S. T.; Oloo, W. N.; Mukherjee, A.; Que, L., Jr. *Inorg. Chem.* **2015**, *54*, 5053–5064.

(18) Krebs, C.; Galonić Fujimori, D.; Walsh, C. T.; Bollinger, J. M. *Acc. Chem. Res.* **2007**, *40*, 484–492.

(19) De Visser, S. P. *J. Am. Chem. Soc.* **2006**, *128*, 9813–9824.

(20) Hirao, H.; Kumar, D.; Que, L., Jr.; Shaik, S. J. *Am. Chem. Soc.* **2006**, *128*, 8590–8606.

(21) Chen, K.; Que, L., Jr. *J. Am. Chem. Soc.* **2001**, *123*, 6327–6337.

(22) Company, A.; Gómez, L.; Güell, M.; Ribas, X.; Luis, J. M.; Que, L., Jr.; Costas, M. *J. Am. Chem. Soc.* **2007**, *129*, 15766–15767.

(23) Prat, I.; Company, A.; Postils, V.; Ribas, X.; Que, L., Jr.; Luis, J. M.; Costas, M. *Chem. - Eur. J.* **2013**, *19*, 6724–6738.

(24) Company, A.; Gómez, L.; Fontrodona, X.; Ribas, X.; Costas, M. *Chem. - Eur. J.* **2008**, *14*, 5727–5731.

(25) Bassan, A.; Blomberg, M. R. A.; Siegbahn, P. E. M.; Que, L., Jr. *Chem. - Eur. J.* **2005**, *11*, 692–705.

(26) Hitomi, Y.; Arakawa, K.; Funabiki, T.; Kodera, M. *Angew. Chem., Int. Ed.* **2012**, *51*, 3448–3452.

(27) Tiago de Oliveira, F.; Chanda, A.; Banerjee, D.; Shan, X.; Mondal, S.; Que, L., Jr.; Bominaar, E. L.; Münck, E.; Collins, T. J. *Science* **2007**, *315*, 835–838.

(28) Ghosh, M.; Singh, K. K.; Panda, C.; Weitz, A.; Hendrich, M. P.; Collins, T. J.; Dhar, B. B.; Gupta, S. S. *J. Am. Chem. Soc.* **2014**, *136*, 9524–9527.

(29) Kwon, E.; Cho, K.-B.; Hong, S.; Nam, W. *Chem. Commun.* **2014**, *50*, 5572–5575.

(30) Noack, H.; Siegbahn, P. E. M. *J. Biol. Inorg. Chem.* **2007**, *12*, 1151–1162.

(31) Cho, K. B.; Wu, X.; Lee, Y. M.; Kwon, Y. H.; Shaik, S.; Nam, W. *J. Am. Chem. Soc.* **2012**, *134*, 20222–20225.

(32) Comba, P.; Maurer, M.; Vadeivelu, P. *J. Phys. Chem. A* **2008**, *112*, 13028–13036.

(33) Frisch, M. J.; Trucks, G. W.; Schlegel, H. B.; Scuseria, G. E.; Robb, M. A.; Cheeseman, J. R.; Scalmani, G.; Barone, V.; Mennucci, B.; Petersson, G. A.; Nakatsuji, H.; Caricato, M.; Li, X.; Hratchian, H. P.; Izmaylov, A. F.; Bloino, J.; Zheng, G.; Sonnenberg, J. L.; Hada, M.; Ehara, M.; Toyota, K.; Fukuda, R.; Hasegawa, J.; Ishida, M.; Nakajima, T.; Honda, Y.; Kitao, O.; Nakai, H.; Vreven, T., Jr.; Peralta, J. E.; Ogliaro, F.; Bearpark, M.; Heyd, J. J.; Brothers, E.; Kudin, K. N.; Staroverov, V. N.; Kobayashi, R.; Normand, J.; Raghavachari, K.; Rendell, A.; Burant, J. C.; Iyengar, S. S.; Tomasi, J.; Cossi, M.; Rega, N.; Millam, J. M.; Klene, M.; Knox, J. E.; Cross, J. B.; Bakken, V.; Adamo, C.; Jaramillo, J.; Gomperts, R.; Stratmann, R. E.; Yazyev, O.; Austin, A. J.; Cammi, R.; Pomelli, C.; Ochterski, J. W.; Martin, R. L.; Morokuma, K.; Zakrzewski, V. G.; Voth, G. A.; Salvador, P.; Dannenberg, J. J.; Dapprich, S.; Daniels, A. D.; Farkas, Foresman, J. B.; Ortiz, J. V.; Cioslowski, J.; Fox, D. J. *Gaussian 09*, Revision A.02; Gaussian Inc.: Wallingford, CT, 2009.

(34) Becke, A. J. *Chem. Phys.* **1993**, *98*, 5648–5652.

(35) Lee, C.; Yang, W.; Parr, R. G. *Phys. Rev. B: Condens. Matter Mater. Phys.* **1988**, *37*, 785–789.

(36) Dolg, M.; Wedig, U.; Stoll, H.; Preuss, H. *J. Chem. Phys.* **1987**, *86*, 866–872.

(37) Hratchian, H. P.; Schlegel, H. B. *J. Chem. Theory Comput.* **2005**, *1*, 61–69.

(38) Hratchian, H. P.; Schlegel, H. B. *J. Chem. Phys.* **2004**, *120*, 9918–9924.

(39) Yamaguchi, K.; Jensen, F.; Dorigo, A.; Houk, K. N. *Chem. Phys. Lett.* **1988**, *149*, 537–542.

(40) Wittbrodt, J. M.; Schlegel, H. B. *J. Chem. Phys.* **1996**, *105*, 6574–6577.

(41) Grimme, S. *J. Comput. Chem.* **2006**, *27*, 1787–1799.

(42) Marenich, A. V.; Cramer, C. J.; Truhlar, D. G. *J. Phys. Chem. B* **2009**, *113*, 6378–6396.

(43) Ribeiro, R. F.; Marenich, A. V.; Cramer, C. J.; Truhlar, D. G. *J. Phys. Chem. B* **2011**, *115*, 14556–14562.

(44) Scholes, G. D.; Curutchet, C.; Mennucci, B.; Cammi, R.; Tomasi, J. *J. Phys. Chem. B* **2007**, *111*, 6978–6982.

- (45) *Advances in Chemical Physics*; Prigogine, I., Rice, S. A., Eds.; John Wiley & Sons, Inc.: Hoboken, NJ, USA, 1999; Vol. 106.
- (46) Marcus, R. A. *J. Chem. Phys.* **1956**, *24*, 966–978.
- (47) Perdew, J. P.; Zunger, A. *Phys. Rev. B: Condens. Matter Mater. Phys.* **1981**, *23*, 5048–5079.
- (48) Zhang, Y.; Yang, W. *J. Chem. Phys.* **1998**, *109*, 2604–2608.
- (49) Lundberg, M.; Siegbahn, P. E. M. *J. Chem. Phys.* **2005**, *122*, 224103.
- (50) Johansson, A. J.; Blomberg, M. R. A.; Siegbahn, P. E. M. *J. Chem. Phys.* **2008**, *129*, 154301.
- (51) Swart, M.; Groenhof, A. R.; Ehlers, A. W.; Lammertsma, K. *J. Phys. Chem. A* **2004**, *108*, 5479–5483.
- (52) Swart, M. *J. Chem. Theory Comput.* **2008**, *4*, 2057–2066.
- (53) Güell, M.; Solà, M.; Swart, M. *Polyhedron* **2010**, *29*, 84–93.
- (54) Radoń, M. *J. Chem. Theory Comput.* **2014**, *10*, 2306–2321.
- (55) Ji, L.; Faponle, A. S.; Quesne, M. G.; Sainna, M. A.; Zhang, J.; Franke, A.; Kumar, D.; van Eldik, R.; Liu, W.; de Visser, S. P. *Chem. - Eur. J.* **2015**, *21*, 9083–9092.
- (56) Harvey, J. N.; Aschi, M.; Schwarz, H.; Koch, W. *Theor. Chem. Acc.* **1998**, *99*, 95–99.
- (57) Acuña-Parés, F.; Codolà, Z.; Costas, M.; Luis, J. M.; Lloret-Fillol, J. *Chem. - Eur. J.* **2014**, *20*, 5696–5707.
- (58) Acuña-Parés, F.; Costas, M.; Luis, J. M.; Lloret-Fillol, J. *Inorg. Chem.* **2014**, *53*, 5474–5485.
- (59) Codolà, Z.; Garcia-Bosch, I.; Acuña-Parés, F.; Prat, I.; Luis, J. M.; Costas, M.; Lloret-Fillol, J. *Chem. - Eur. J.* **2013**, *19*, 8042–8047.
- (60) Prat, I.; Mathieson, J. S.; Güell, M.; Ribas, X.; Luis, J. M.; Cronin, L.; Costas, M. *Nat. Chem.* **2011**, *3*, 788–793.
- (61) Karamzadeh, B.; Singh, D.; Nam, W.; Kumar, D.; de Visser, S. P. *Phys. Chem. Chem. Phys.* **2014**, *16*, 22611–22622.
- (62) De Visser, S. P.; Tan, L. S. *J. Am. Chem. Soc.* **2008**, *130*, 12961–12974.
- (63) Kumar, S.; Faponle, A. S.; Barman, P.; Vardhaman, A. K.; Sastri, C. V.; Kumar, D.; de Visser, S. P. *J. Am. Chem. Soc.* **2014**, *136*, 17102–17115.
- (64) Zavitsas, A. A. *J. Org. Chem.* **2008**, *73*, 9022–9026.
- (65) De Visser, S. P. *J. Am. Chem. Soc.* **2010**, *132*, 1087–1097.
- (66) Kumar, D.; Karamzadeh, B.; Sastry, G. N.; de Visser, S. P. *J. Am. Chem. Soc.* **2010**, *132*, 7656–7667.
- (67) Kumar, D.; Latifi, R.; Kumar, S.; Rybak-Akimova, E. V.; Sainna, M. A.; de Visser, S. P. *Inorg. Chem.* **2013**, *52*, 7968–7979.
- (68) Ye, S.; Geng, C.-Y.; Shaik, S.; Neese, F. *Phys. Chem. Chem. Phys.* **2013**, *15*, 8017–8030.
- (69) Decker, A.; Rohde, J.-U.; Klinker, E. J.; Wong, S. D.; Que, L., Jr.; Solomon, E. I. *J. Am. Chem. Soc.* **2007**, *129*, 15983–15996.
- (70) Sahu, S.; Widger, L. R.; Quesne, M. G.; De Visser, S. P.; Matsumura, H.; Moëne-Loccoz, P.; Siegler, M. A.; Goldberg, D. P. *J. Am. Chem. Soc.* **2013**, *135*, 10590–10593.
- (71) Tsuzuki, S. *Annu. Rep. Prog. Chem., Sect. C: Phys. Chem.* **2012**, *108*, 69–95.
- (72) Alamiddine, Z.; Humbel, S. *Front. Chem.* **2014**, *1*, 37.
- (73) Kozuch, S.; Shaik, S. *Acc. Chem. Res.* **2011**, *44*, 101–110.
- (74) Houle, F. A.; Beauchamp, J. L. *J. Am. Chem. Soc.* **1979**, *101*, 4067–4074.
- (75) Janardanan, D.; Usharani, D.; Chen, H.; Shaik, S. *J. Phys. Chem. Lett.* **2011**, *2*, 2610–2617.

NOTE ADDED AFTER ASAP PUBLICATION

After this paper was published ASAP August 19, 2015, Figure 4 was replaced. The corrected version was reposted August 24, 2015.